Key Points:
- Modeled subglacial channel networks grow inland from the ice sheet margin and over bedrock ridges
- An inverse relationship between effective pressure and surface speed is observed in the mid-melt season when surface speeds are high
- Driving stress is likely the dominant control on surface speed outside of the mid-melt season

Relationship Between Greenland Ice Sheet Surface Speed and Modeled Effective Pressure

Laura A. Stevens[1,2] (iD), **Ian J. Hewitt[3]** (iD), **Sarah B. Das[4]** (iD), and **Mark D. Behn[4]** (iD)

[1]Massachusetts Institute of Technology/Woods Hole Oceanographic Institution Joint Program in Oceanography/Applied Ocean Science and Engineering, Woods Hole, MA, USA, [2]Now at Lamont-Doherty Earth Observatory, Columbia University, Palisades, NY, USA, [3]Mathematical Institute, University of Oxford, Oxford, UK, [4]Department of Geology and Geophysics, Woods Hole Oceanographic Institution, Woods Hole, MA, USA

Abstract We use a numerical subglacial hydrology model and remotely sensed observations of Greenland Ice Sheet surface motion to test whether the inverse relationship between effective pressure and regional melt season surface speeds observed at individual sites holds on a regional scale. The model is forced with daily surface runoff estimates for 2009 and 2010 across an ~8,000-km^2 region on the western margin. The overall subglacial drainage system morphology develops similarly in both years, with subglacial channel networks growing inland from the ice sheet margin and robust subglacial pathways forming over bedrock ridges. Modeled effective pressures are compared to contemporaneous regional surface speeds derived from TerraSAR-X imagery to investigate spatial relationships. Our results show an inverse spatial relationship between effective pressure and ice speed in the mid-melt season, when surface speeds are elevated, indicating that effective pressure is the dominant control on surface velocities in the mid-melt season. By contrast, in the early and late melt seasons, when surface speeds are slower, effective pressure and surface speed have a positive relationship. Our results suggest that outside of the mid-melt season, the influence of effective pressures on sliding speeds may be secondary to the influence of driving stress and spatially variable bed roughness.

1. Introduction

Understanding the physical processes driving variability in ice sheet flow is a persistent challenge that hinders our prediction of sea level rise contributions from Greenland Ice Sheet mass loss (Pritchard et al., 2009; Vaughan et al., 2013). Outside of the fast-flowing trunks of outlet glaciers, seasonal acceleration of the ablation zone is observed to coincide with surface melting across the Greenland Ice Sheet, though the amount of net annual ice motion is largely insensitive to (or in some cases inversely related to) the magnitude of annual melt (Joughin et al., 2013, 2008; Stevens, Behn, et al., 2016; Sole et al., 2013; Tedstone et al., 2015; van de Wal et al., 2008, 2015; Zwally et al., 2002). The spatiotemporal variability of surface meltwater reaching and traveling along the ice-bed interface is frequently hypothesized to play a major role in controlling ice sheet velocities through its ability to *lubricate* the ice-bed interface (e.g., Andrews et al., 2014; Das et al., 2008; Hoffman et al., 2011; Ryser et al., 2014; Schoof, 2010; Shepherd et al., 2009; Smith et al., 2015; Stevens et al., 2015; Wright et al., 2016). However, a quantitative understanding of this control is lacking due to the difficulties in making direct geophysical observations at the ice-bed interface.

Numerical models paired with surface observations provide a means to test theories relating ice flow to subglacial water routing (Flowers, 2015). However, recent progress in developing models of the subglacial drainage system has been largely divorced from regional measurements of ice surface velocity. Currently, time-evolving subglacial hydrology models often use idealized ice sheet geometries (Hewitt, 2013; Hoffman & Price, 2014; Schoof, 2010), time-invariant hydraulic potential to fix the locations of subglacial channels (Banwell et al., 2013), and/or calibrate models that are thousands of square kilometers in area to a few point-source Global Positioning System (GPS) velocity, GPS uplift, or borehole measurements (de Fleurian et al., 2016; Hoffman et al., 2016). While regional observations and measurements are most useful for model calibration (Flowers, 2015), only a few regional observations of the spatiotemporal evolution of ice flow through the melt season exist for the Greenland margin (Bougamont et al., 2014; Joughin et al., 2013; Palmer et al., 2011). From these few regional observations, the location of surface speedup has been shown to align with observed supraglacial catchments (Joughin et al., 2013; Palmer et al., 2011) and modeled
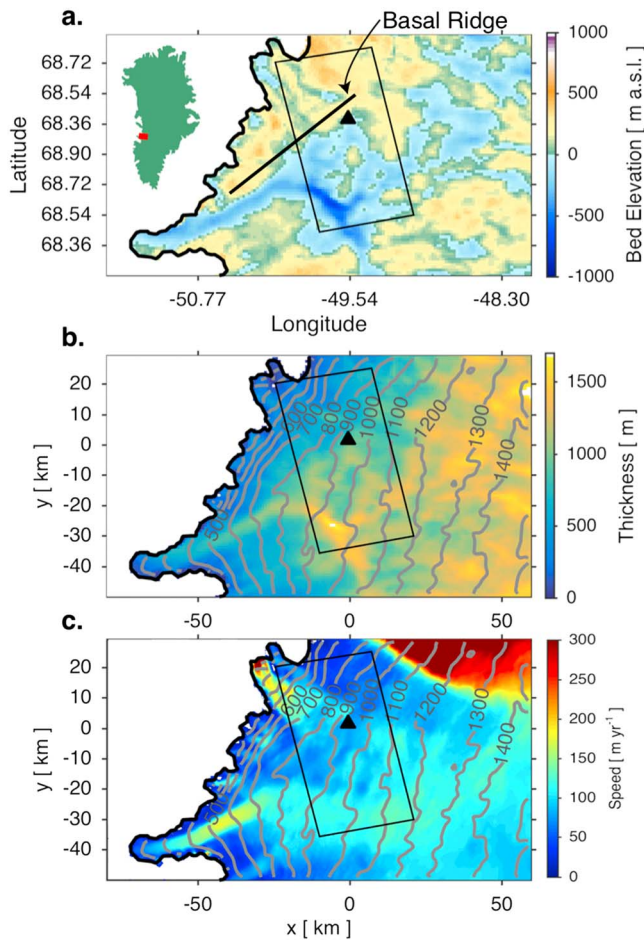
Figure 1. Model domain. (a) Bedrock topography of the model domain, with ice sheet margin outlined in black. Black triangle marks the location of North Lake (Das et al., 2008). Black line marks location of prominent basal ridge. Black rectangle is the area outline of the flow speed maps in Figure 2. (b) Ice sheet thickness of the model domain. Gray contour lines show 100-m surface ice elevation contours. (c) Average winter flow speed from the MEaSUREs Multi-year Greenland Ice Sheet Velocity Mosaic (Version 1) from Joughin et al. (2010, 2016, 2017).

subglacial drainage pathways (Bougamont et al., 2014; Chu et al., 2016). However, more work is needed to enable models of basal sliding to resolve these observations (Flowers, 2015).

In the ablation zone of the Greenland Ice Sheet, basal sliding can account for as much as 90% of ice motion in the melt season (Ryser et al., 2014). Pairing subglacial hydrology models with surface velocity observations provides a test of theoretical parameterizations for basal sliding. Though there are many functional forms, most models for basal sliding, u_b, take the general form: $\tau_b = f(u_b, N)$, where τ_b is basal shear stress and N is effective pressure (ice overburden pressure minus the water pressure; Cuffey & Patterson, 2010; Fowler, 1987; Iken & Bindschadler, 1986; Schoof, 2010). With f an increasing function of both u_b and N, surface speed should vary inversely with effective pressure for a given τ_b. In interior regions of the ice sheet where longitudinal and wall stresses provide little resistance to flow, τ_b is approximately equal to the driving stress, τ_d (Cuffey & Patterson, 2010). Some ice sheet flow models have made use of this form of sliding law to couple ice dynamics to subglacial hydrology through model-derived effective pressures (Bougamont et al., 2014; Hewitt, 2013; Hoffman et al., 2016; Schoof, 2010). However, whether the inverse relationship between effective pressure and regional melt season surface speeds observed at individual sites holds on a regional scale with variable basal shear stress has not been tested using available observational data sets.

In this study, we use a 900-m resolution regional subglacial hydrology model to evaluate whether the inverse relationship between model-derived effective pressures and observed ice surface speeds during the summer melt season holds spatially across a range of driving stresses. This question tests a combination of model and theory justified on the basis that (1) we do not have widespread *measurements* of effective pressure and (2) we expect that if the theory is to be used, it will be in combination with a model used to predict effective pressures. The model incorporates (1) distributed and channelized subglacial drainage components, (2) real ice sheet topography and ice thickness, and (3) daily resolved surface runoff inputs. Our study area (Figure 1) is a region that has previously been shown to exhibit spatiotemporally complex seasonal surface speeds in 2009 and 2010 (Figure 2; Joughin et al., 2013). Comparing the predictions of the subglacial hydrology model with these regional surface speed observations, we find an inverse spatial relationship between effective pressure and ice velocity in the mid-melt season and a positive relationship in the early and late melt seasons. Our results imply that effective pressure is the dominant control on surface velocities in the mid-melt season. Outside of the mid-melt season, spatially variable controls on sliding that are not solely due to effective pressure (e.g., bed roughness, and sediment thickness) may be important to include when applying a sliding law in regional scale coupled models of subglacial hydrology and ice flow.

2. Methods

2.1. Study Region

We focus our study on an 8,110-km^2 area of both fjord- and land-terminating ice located immediately south of Jakobsahvn Isbræ in western Greenland (Figure 1a). This study area ranges ~100 km inland from the ice margin and is characterized by three slow-moving (~150 m/year) marine-terminating outlet glaciers (Joughin et al., 2013), shallow ice sheet surface slopes, and numerous supraglacial rivers and lakes (Yang et al., 2015; Figure 1b). The entirety of the region is within the ablation zone, with the local equilibrium line altitude at ~1,500 m above sea level (Poinar et al., 2016).
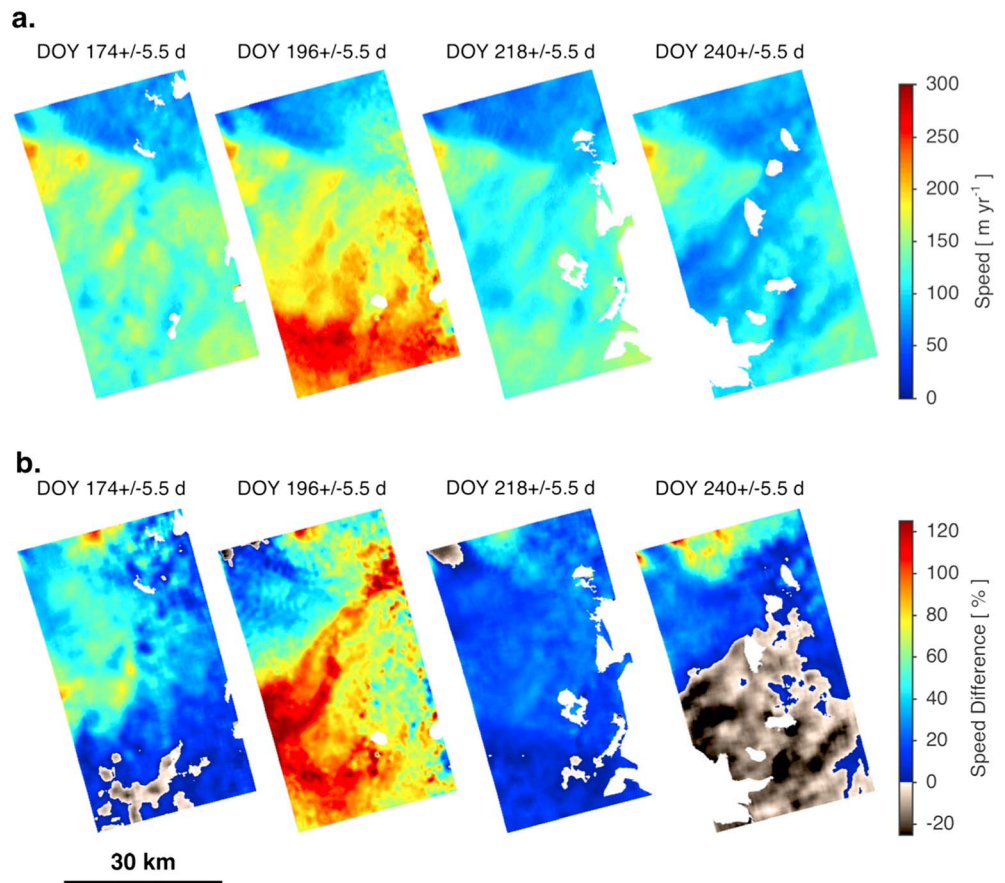
Figure 2. The 2009 ice sheet velocities. (a) Summer 2009 flow speeds from 11-day interval TerraSAR-X images. The date at the top of the panel corresponds to the central date for the 11-day interval over which the velocity was determined. (b) Increase in summer 2009 flow speeds relative to the 2007–2009 winter speed (Figure 1c) plotted as a percentage difference of the winter speed. The date at the top of the panel corresponds to the central date for the 11-day interval over which the velocity was determined. Data are from Joughin et al. (2013). DOY = day of year.

The region was chosen based on the availability of in situ and remotely sensed ice sheet velocity data (Das et al., 2008; Joughin et al., 2013, 2008; Stevens, Behn, et al., 2016; Stevens et al., 2015; Stevens, Straneo, et al., 2016) and high-resolution basal topography derived from radar data sets (Bamber et al., 2013; Morlighem et al., 2014). Regional surface velocity measurements over the 2009 and 2010 melt seasons derived from 11-day repeat TerraSAR-X images reveal a spatiotemporally complex pattern of speedup (Figures 2a and 2b; Joughin et al., 2010, 2013). These velocity maps cover 1,700 km^2 (~20%) of the study region (Figure 1c) and provide one of the first data sets of spatially extensive ice sheet surface speeds that can be compared with the outputs of our subglacial hydrology model. A previous time-invariant model of subglacial water flow in this region calculated using theoretical, static hydraulic potential fields by Chu et al. (2016) provides an additional model comparison study.

2.2. Subglacial Hydrology Model

We use the two-dimensional model of subglacial drainage employed by Banwell et al. (2016) and originally developed by Hewitt (2013). The model routes ice sheet surface meltwater input into a continuous *sheet* connected to discrete *channels* melted upward into the base of the ice sheet (Hewitt, 2013). Water moves between a continuous sheet, channels, and englacial storage to maintain a continuous hydraulic potential ϕ (Figure 3). The model is forced by daily surface runoff R derived from a regional climate model (section 2.2.2). Model governing equations and numerical procedure are given in supporting information Texts S1 and S2.
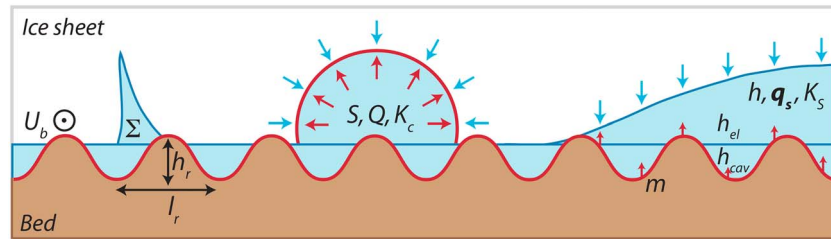
Figure 3. Cross-section schematic of subglacial hydrology model. From left to right, the schematic depicts englacial storage Σ, channels, and cavities of the subglacial hydrology model. The cavity sheet h_{cav} and elastic sheet h_{el} sum to the thickness of the continuous sheet h. The cavity layer h_{cav} is bounded by bed undulations of height scale h_r and length scale l_r. Melt (red arrows) and creep closure (blue arrows) control the growth and decay of channel and cavity elements. The schematic is not to scale.

Water flux through the sheet $\boldsymbol{q_s}$ is dependent on the coefficient K_s controlling the sheet permeability, and sheet thickness h, which is the sum of two components: a cavity sheet of thickness h_{cav} and an elastic sheet of thickness h_{el} (Figure 3). The thickness of the cavity sheet h_{cav} represents the height of water-filled cavities (Creyts & Schoof, 2009; Schoof et al., 2012) and evolves due to the combined effects of basal ice melt and cavity opening by basal sliding and cavity closing by ice creep. The elastic sheet height is included to represent the elastic uplift or *hydraulic jacking* of ice where the effective pressure N becomes negative ($N = p_i - p_w$, where p_i is the ice overburden pressure and p_w is the water pressure). Water in the sheet is connected to discrete channels with cross-sectional area S, discharge Q, and turbulent flow coefficient K_c. The growth and decay of channel cross-sectional area are governed by the competing effects of melt back and creep closure of channel walls. The incipient sheet width contributing to channel melting λ_c sets the length scale over which ice melting contributes to channel formation.

Our primary focus is on the model predictions of total flux q (the combined flux from both the channel and sheet layers) and effective pressure N, which are solved at every model grid point. We further distinguish whether the drainage system morphology is inefficient (majority of drainage through linked cavities) or efficient (majority of drainage through channels). We define efficient drainage based on the conditions $N > 0$ MPa and $q > 0.001$ m²/s, which is similar to defining the drainage system based on the fraction of flow in the channel layer. Because the exact form of the sliding law is uncertain and can be highly nonlinear, the ice flow model in Hewitt (2013) is not employed here. Instead, we compare ice surface speed directly to effective pressure N in order to quantify this relationship both spatially and temporally over multiple seasonal cycles.

2.2.1. Model Domain and Boundary Conditions

The model domain is shown in Figure 1. Bedrock topography is calculated from the IceBridge BedMachine Greenland Version 2 bedmap available at the National Aeronautics and Space Administration National Snow and Ice Data Center (https://doi.org/10.5067/AD7B0HQNSJ29; Morlighem et al., 2014). Bed elevations are assigned to the regularly spaced, 900-m mesh of model nodes by subsampling the Morlighem et al. (2014) bed map at every sixth point (Figure 1a). Ice sheet surface elevation is calculated from the Greenland Ice Mapping Project digital elevation model (Howat et al., 2014) with equivalent subsampling to that of the bed elevations. Given that the bedrock topography and ice sheet shape change minimally over the course of a few years (Hewitt, 2013), the bed and ice sheet surface geometries are assumed to be fixed.

The model is forced with daily runoff from 1 January 2008 to 31 December 2010. At the start of the model run (1 January 2008), initial hydraulic potential ϕ conditions at the bed are set by prescribing p_w such that ϕ is equivalent to 90% of overburden pressures. The initial condition for cavity sheet thickness h_{cav} is calculated from the steady state form of equation (S3). A background basal melt rate, m, is prescribed everywhere to be 0.0059 m/year based on the average geothermal heat flux of 0.063 W/m² beneath Greenland (Rogozhina et al., 2012; equation (S4)). We neglect basal melt from frictional sliding, which would depend on the choice of sliding law. However, sensitivity tests show that there is little difference between simulations with and without a frictional heating term. This result is consistent with the fact that surface runoff comprises ~99% of the meltwater input to the model domain (section 4.4.4).

The seasonal cycles in the runoff forcing prevent the model from reaching a steady state. Moreover, for some parameter choices, regions of elevated water flux persist from the end of one runoff season until the beginnings of the following year's runoff season. Thus, we use 2008 as a *spin-up* year and focus on the evolution of the drainage system in 2009 and 2010. The use of one spin-up year is justified based on the similarity in discharge morphology and timing in 2009 and 2010 after testing the model with both one 2008 spin-up year and with two 2008 spin-up years.

At the domain boundaries under interior ice, a no melt flux condition is applied. An upstream basal melt flux term was omitted after confirming that it had little effect on the model output in our study region. At both marine- and land-terminating margins of the ice sheet, we prescribe $N = 0$. This boundary condition is appropriate for land-terminating margins so long as ice sheet thickness tapers to zero at the margin (Figure 1b) and represents approximately hydrostatic pressure at marine-terminating margins. Boundary nodes along the ice sheet margin are dynamically adjusted at each 1-day time step. If there is inflow at the node, pressure is no longer prescribed at that node and a no flux condition is applied instead. This prevents water from getting sucked under the ice sheet from submarine regions outside of the model domain. If the pressure predicted becomes larger than the boundary pressure, the condition is switched back to a pressure outlet condition.

2.2.2. Surface Runoff Forcing

Surface runoff is estimated from the daily, downscaled 1-km resolution Regional Atmospheric Climate Model v. 2.3 (Noël et al., 2016, 2015). The subglacial model is forced with one of two forms of surface runoff input such that the ice sheet bed receives either (1) inputs at every model node (distributed) or (2) inputs at assigned points (discrete). Discrete input more accurately reflects observed surface hydrology on the ice sheet (Chu, 2013), whereas the distributed input scenario is used to test the model sensitivity to prescribed moulin locations and meltwater flux.

In the distributed input scenario, Regional Atmospheric Climate Model daily runoff values are interpolated to each of the model grid nodes. In the discrete input formation, the runoff values are accumulated from catchment basins surrounding prescribed elevation-dependent moulin locations, resulting in 20% or fewer of the grid cells receiving direct surface input (method fully described in supporting information Text S3). In both scenarios there is no surface storage, and runoff immediately transits to the bed. The total meltwater input to the bed is equivalent in both cases.

2.3. Comparison of Ice Sheet Surface Speeds to Model Output and Static Variables.

To compare ice sheet surface speeds to model output, we first calibrate the model parameter space over the three parameters that most greatly affect the timing and morphology of the subglacial drainage system (section 2.3.1). We then evaluate the dominant control on melt season surface speeds through weighted linear regression (section 2.3.2) and coherence estimation (section 2.3.3) against static variables (driving stress, bed elevation, surface slope, and ice sheet thickness) and evolving variables (runoff, effective pressure).

2.3.1. Parameter Space Calibration

Nonvarying model parameter values are taken from Banwell et al. (2016; Table S1). We vary three parameters —K_s, λ_c, and σ—which were identified in previous model studies (Banwell et al., 2016; Hewitt, 2013; Werder et al., 2013) as most greatly affecting the timing and morphology of the inefficient and efficient subglacial drainage systems. We vary the following: sheet permeability K_s by factors of 10 across the range $10^{-4} \leq K_s \leq 10^{-2}$ $Pa^{-1}s^{-1}$; width of the sheet that contributes to channel melting λ_c across the range $\lambda_c = [100, 1,000, \text{and } 5,000]$ m; and englacial void fraction σ by factors of 10 across the range $10^{-4} \leq \sigma \leq 10^{-2}$. This results in 27 different parameter combinations for each of the surface melt forcing scenarios (distributed or discrete).

To test the relationship between model-derived effective pressures and observed surface speeds, we need a way to calibrate the parameter space that is independent of surface velocity measurements. Previous studies of land-terminating ice using this model assessed parameter space fitness by comparing measured proglacial discharge at stream discharge stations (Banwell et al., 2016; Hewitt, 2013; Werder et al., 2013). Proglacial discharge from our study area enters into unmonitored proglacial lakes and fjords, requiring an alternative approach.

Vertical ice surface motion from a multiyear network of GPS receivers in the center of our study region provides a potentially useful constraint on the timing of inefficient to efficient drainage system

transition that it is independent of the surface velocity measurements. In particular, records collected during multiple years of rapid drainages of supraglacial lake North Lake ((0,0) km in model domain) demonstrate contrasting surface ice uplift responses (Das et al., 2008; Stevens, Behn, et al., 2016; Stevens et al., 2015) that we infer to be a response to the timing of the inland migration of an efficient drainage system. To first order, we interpret a longer period (>24 hr) of sustained uplift following a lake drainage event to reflect that an inefficient subglacial drainage system exists locally, whereas a short period of uplift (<24 hr) suggests that the drainage system had already evolved to become efficient. This interpretation is further supported by a numerical model of North Lake drainage where basal water pressures subside to predrainage levels within 24 hr of the drainage event when sufficiently large preexisting channels characteristic of an efficient drainage system are present (Pimentel & Flowers, 2010). We bracket this transition using 2 years with contrasting responses (2006 and 2009) that are otherwise similar in total melt season runoff magnitude and day of runoff onset (Stevens, Behn, et al., 2016). In 2009, North Lake drained on day of year (DOY) 168 resulting in sustained surface uplift (Figure S3). In contrast, ice sheet surface elevations at the same location subsided to predrainage elevations within 24 hr after the late melt season 2006 drainage on DOY 210 (Das et al., 2008; Figure S3). Thus, we use the dates DOYs 168 and 210 as bounds for the inland migration of an efficient drainage system. We acknowledge the 40 days between the calendar dates of the 2006 and 2009 lake drainage events comprises a large portion of the melt season, making this parameter space criterion rather imprecise. The primary justification for using this criterion is that it is independent of the surface velocity measurements that we will later compare to modeled effective pressures, and it is better than nothing.

2.3.2. Regression of Surface Speeds to Model Output and Static Variables

We perform weighted linear regressions to determine the relationships between surface speeds, static variables, and modeled effective pressures. For the weighted linear regression analysis, 11-day averages of runoff R, total flux q, and effective pressure N are calculated for each node within the TerraSAR-X region over the equivalent time intervals of the TerraSAR-X data. The 11-day averages of N are interpolated to the 100-m resolution TerraSAR-X grid and plotted against the TerraSAR-X ice sheet surface speed. Scatter plots are linearly discretized along the N and speed axis; speed averages are calculated within each bin along N. A weighted linear least squares regression is performed, using two standard deviations of the binned surface speed measurement as the weight on the y values. The correlation coefficient, r, of the weighted least squares regression is taken as a measurement of the linear relationship between N and speed.

An equivalent procedure is used to quantify the relationships between driving stress τ_d and speed, runoff and speed, bed elevation and speed, ice sheet surface slope and speed, and ice sheet thickness and speed. τ_d is calculated according to

$$\tau_d = \rho_i g H \sin(\alpha), \tag{1}$$

where g is the gravitational acceleration, H is the ice sheet thickness, and α is the ice sheet surface slope averaged over 6 km (~4 ice thicknesses; Figure S4; Cuffey & Patterson, 2010).

2.3.3. Coherence and Spectral Estimation

We use two-dimensional coherence estimates to compare goodness of fit between surface speeds, static variables, and model output effective pressures. Coherence is a bivariate statistic in the spectral domain that is analogous to correlation in the spatial domain (Simons et al., 2000). Coherence measures the phase relationship between two signals, with high coherence values indicating constructive interference at wavenumbers where the two signals are correlated (Kirby, 2014). We follow the methodology and analysis routines of Simons et al. (2000) for estimating two-dimensional coherence of stationary fields (see supporting information Text S4 for full details).

For two stochastic fields (e.g., surface ice velocity (X) and bedrock topography (Y)), the coherence-square function between the two fields, γ_{XY}^2, is the ratio between the magnitude of the fields' cross-spectral density and the power spectral density of the individual fields. Like correlation estimates, coherence-square estimates range from $0 \leq \gamma_{XY}^2 \leq 1$, with $\gamma_{XY}^2 = 1$ indicating an entirely consistent phase relationship between both fields (Simons et al., 2003). Isotropic coherence-square estimates, $\gamma^2(|\mathbf{k}|)$, are calculated by averaging over 360° of azimuth around logarithmically spaced annuli in the wavenumber domain, $\mathbf{k}$ (Kirby, 2014). As the coherence-square estimate is a statistic, the variance of the isotropic coherence-square estimate is

calculated following the Cramer-Rao lower bound (Seymour & Cumming, 1994; Simons et al., 2003). Error estimates of $\gamma^2(|\mathbf{k}|)$ presented throughout the paper are two standard deviations, 2σ. A coherence-square estimation of synthetic data is provided in Figure S5 to illustrate this method.

3. Results

3.1. Seasonal Evolution of Model Output

Model snapshots of runoff, subglacial water flux, and effective pressure (Figure 4) illustrate drainage system evolution through the melt season. Surface runoff begins in the early melt season in the lower elevations of the domain (Figure 4b), with effective pressures decreasing as runoff input to the bed overwhelms cavities of the inefficient drainage system of the winter and spring. Channels grow inland from the ice sheet margin over the melt season, and effective pressures increase and eventually surpass their pre–melt season values with the establishment of an efficient drainage system (Figures 4c–4e). A similar inland drainage system evolution is observed in both the distributed (Figure 4) and discrete (Figure 5) runoff input scenarios.

As effective pressures increase with channel formation (Schoof, 2010), the inefficient to efficient drainage system transition can be observed spatially by tracking the band of 0-MPa effective pressure N values, which moves inland from the early melt season onward (Figure 4c). Between the ice sheet margin and the 0-MPa effective pressure values, effective pressures are high ($N > 0$) and subglacial hydrology morphology shows definitive channelization characterized by locations with $q > 0.1$ m^2/s (Figure 3d). Inland of the 0-MPa effective pressure values, effective pressures are low ($N < 0$) and drainage morphology shows minimal channelization characterized by the majority of the area having $q < 0.001$ m^2/s (Figure 3d). For equivalent parameter choices, the transition in drainage system behavior migrates inland more slowly for the discrete input scenario (Figure 5) compared to the distributed input scenario (Figure 4). In both input scenarios, the drainage system transition reaches the position of North Lake when ~40% of the area of the TerraSAR-X region contains efficient drainage pathways (Figures 4d and 5d).

This inland evolution of the drainage system is qualitatively similar to that found in the idealized model geometry of Hewitt (2013), with drainage system morphology further dictated by ice sheet surface and bed topography (Figure 5a; Werder et al., 2013). Neither static (Chu et al., 2016; Stevens, Straneo, et al., 2016) nor evolving (this study) treatments of subglacial water routing predict major subglacial flow under the terminus of Nordenskiöld Gletscher (position (-70, -40) km in model domain; Figures 1, 4, and 5). Channels instead favor ice sheet margin discharge locations to the south and north of the Nordenskiöld outlet glacier and are likely steered to these locations by the steeper ice sheet surface gradients and small basal topographic valleys in these areas (Figures 1a and 1b).

3.2. Timing of Transition to Efficient Drainage System

The timing of the transition from inefficient to efficient drainage system at North Lake (model domain (0,0)) is constrained independently by observations (as described in section 2.3.1) and in model space (as described in section 3.1). This provides a metric for calibration of models with distributed (Figures 6a–6c) and discrete (Figures 6d–6f) surface runoff forcing. Over the course of the 2009 summer, the area of efficient drainage in the TerraSAR-X region increases at different rates based on the choice of input scenario (see discussion in section 3.3 below), and the assumed model parameters, with higher K_s and λ_c leading to faster rates of channelization. Figures 6a–6c depict the relative fraction of the basal drainage system that is efficient assuming an englacial storage fraction (σ) of 0.001 (Figure S6 shows equivalent cases for $\sigma = 0.01$ and 0.0001.).

For models run with distributed runoff forcing, a third (33%) of the models transition from inefficient to efficient drainage system too quickly to be in agreement with the 2009 lake drainage record, while an additional 19% of the models transition too slowly (Figures 6a–6c and S6). The majority of the rejected models employed the highest englacial void fraction of =0.01 and exhibited both too fast (denoted by $>$ in Figures 6 and S6) and too slow (denoted by $<$ in Figure S6) drainage system transition. Channelization behavior in 2010 does not restrict the parameter space much further (Figure S7), with only two additional models with the highest englacial void fraction of $\sigma =0.01$ needing to be discarded (Figures S7a–S7c). We note that channelization behavior in 2010 distributed input models exhibits less variability across K_s and λ_c parameter
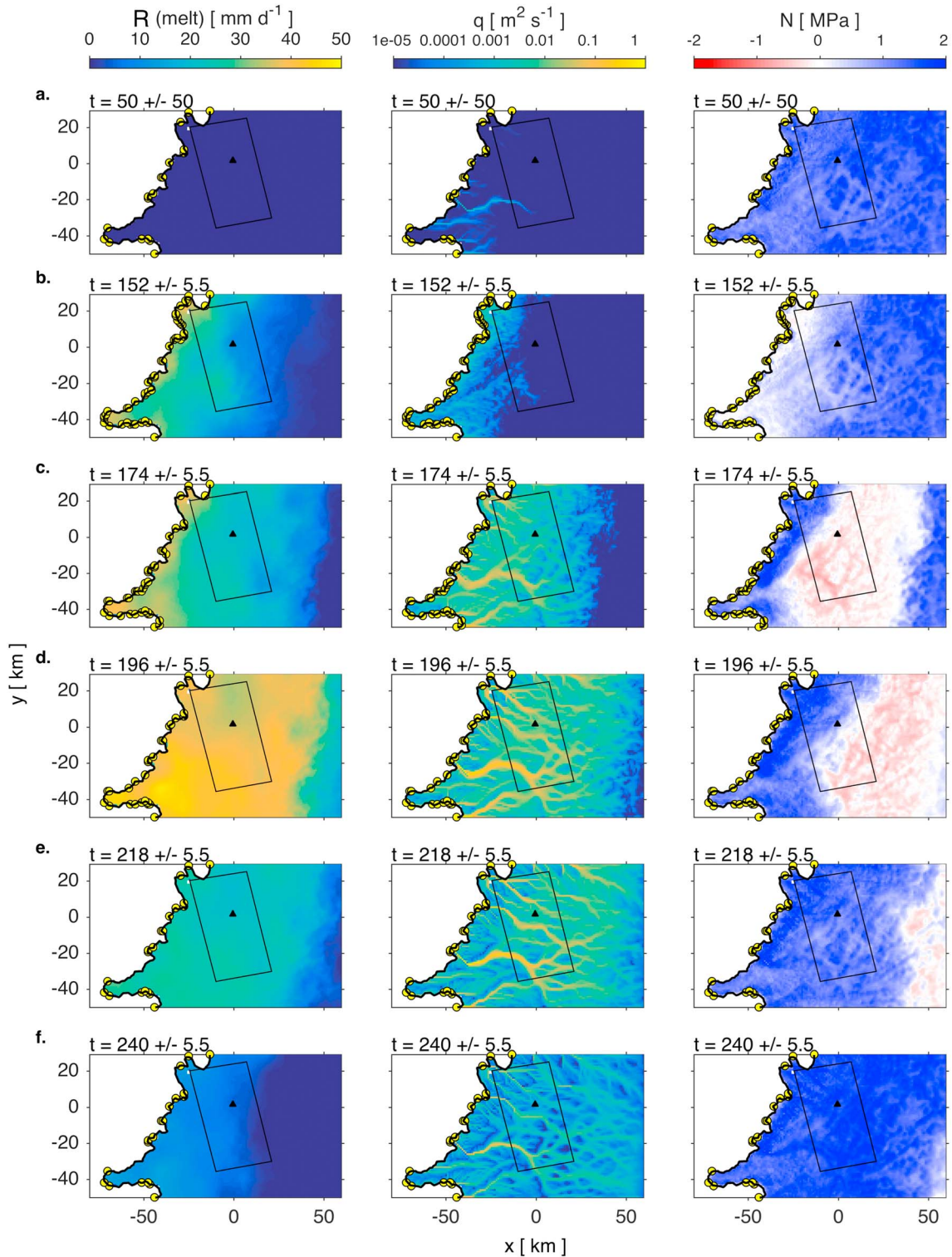
Figure 4. (left column) Averages of surface melt forcing, R (mm/day), (middle column) total node flux, q (m²/s), and (right column) effective pressure, N (MPa), on every node over the 2009 melt season for a distributed surface input scenario. The date at the top of the panel corresponds to the central date for the interval over which the model outputs were determined. The top panels (a) are averages over the first 100 days of the year. The bottom four rows of panels (c)–(f) are 11-day averages corresponding to the dates of summer flow speeds in Figure 2a. Parameters used in this model run are $K_s = 0.001$ Pa^{-1} s^{-1}, $\sigma = 0.001$, and $\lambda_c = 1,000$ m. Black rectangle is the area outline of the ice flow maps in Figure 2. Black triangle marks the location of North Lake. Yellow circles mark discharge outlet locations along the ice sheet margin.
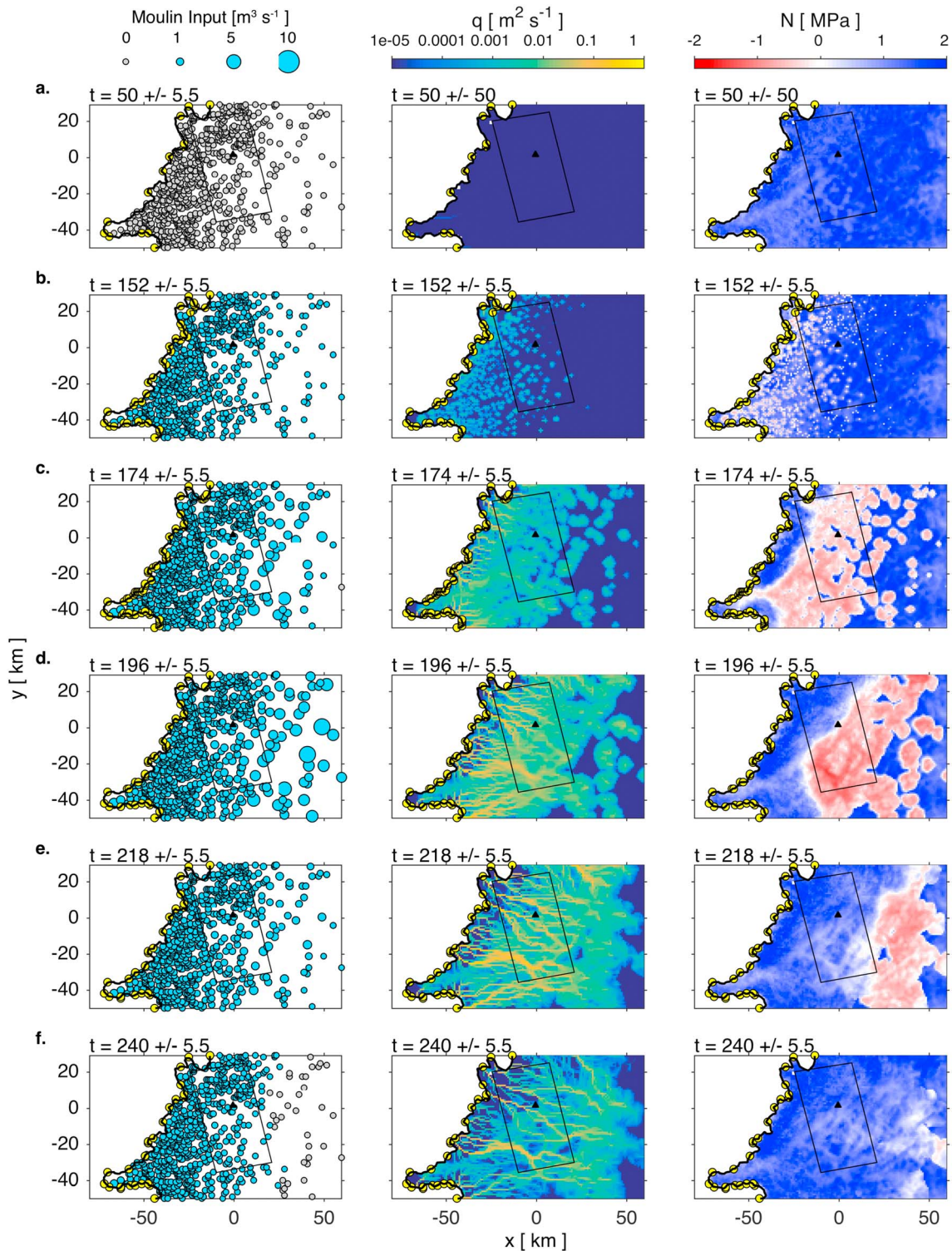
Figure 5. The same as Figure 3 but for a discrete surface input scenario in 2009. Left column is average moulin input (m^3/s).

space (Figure S7), which may be due to the anomalously high surface runoff in 2010. This reduced variability is not caused by preferred discharge morphology developing over multiple model year runs, as we see the same behavior in 2009 and 2010 after testing the model with both one 2008 spin-up year and with two 2008 spin-up years.
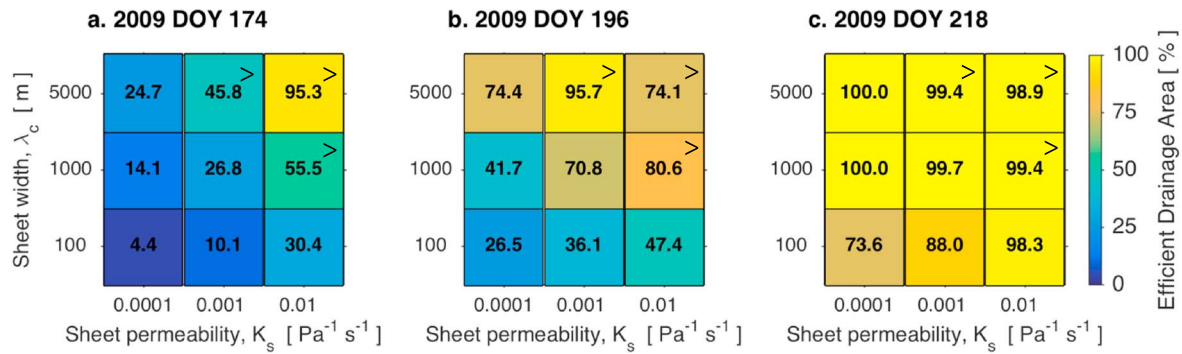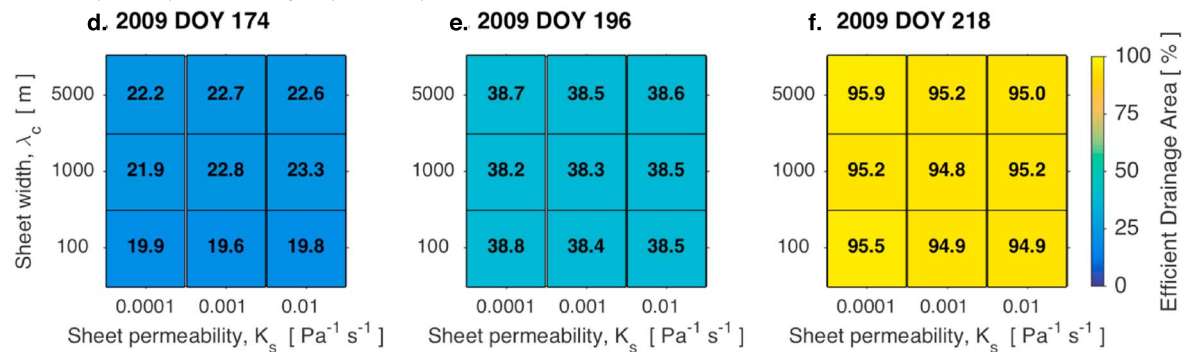
Figure 6. Region of efficient drainage area increases at different rates across model parameter space. Percentage of efficient drainage area across K_s and λ_c parameter space for distributed surface input models on days of year, DOYs, (a) 174, (b) 196, and (c) 218 of 2009. Percentage of efficient drainage area across K_s and λ_c parameter space for discrete surface input models on DOYs (d) 174, (e) 196, and (f) 218 of 2009. Efficient drainage area (EDA) is defined as the area within the TerraSAR-X region where $N > 0$ and $q > 0.001$ m^2/s. The $\sigma = 0.001$ for all models. The $>$ mark models that channelize too quickly with an EDA $> 40\%$ on DOY 174 2009.

We remove the models that do not meet the lake drainage criterion (rejected models denoted by $<$ or $>$ in Figures 6 and S6). Figures 4 and 7–9 show results from a single simulation take from the middle of the parameter space ($K_s = 0.001$ Pa^{-1} s^{-1}, $\lambda_c = 1,000$ m, and $\sigma = 0.001$) that meets the lake drainage criterion. We perform a weighted linear regression across all of the remaining models that meet the lake drainage criterion (48%) and report summary statistics from the discrete input scenario models in Figures 10 and 11.

For models using the discrete runoff forcing, the transition time from inefficient to efficient drainage is largely insensitive to the tested range of K_s and λ_c parameters when $\sigma = 0.001$ (Figures 6d–6f) and $\sigma = 0.0001$ (Figures S8d–S8f). A third (33%) of discrete runoff models were rejected for having unrealistically long lags between surface runoff input and subglacial system channelization in 2009 (Figures S8a–S8c); all of the rejected models employed the highest englacial void fraction of $\sigma = 0.01$. The channelization behavior for 2010 models with discrete surface runoff forcing does not further restrict the parameter space (Figure S9), with slight variations in the timing of the drainage system transition caused by the earlier onset and higher runoff rates in the 2010 melt season. (See section 3.5 below.) Again, we keep all models that meet the lake drainage criterion (66%) for weighted linear regression statistics. For consistency with the distributed scenario, we show the output from the same simulation in the middle of the parameter space ($K_s = 0.001$ Pa^{-1} s^{-1}, $\lambda_c = 1,000$ m, and $\sigma = 0.001$) for plotting purposes in Figures 5, 7, and 8.

3.3. Distributed Versus Discrete Surface Runoff Input

In general, the temporal evolution of the sheet layer and channels is similar between the distributed and discrete models (Figure 7). The onset of runoff in both scenarios (Figure 7a) coincides with increasing height of the sheet layer (Figure 7b) followed by an increase in channel area (Figure 7c). Effective pressures across the domain decrease in the early melt season (Figure 7d), when the majority of water is accommodated in the sheet layer (Figure 7b). As the amount of water accommodated in channels increases and the region of
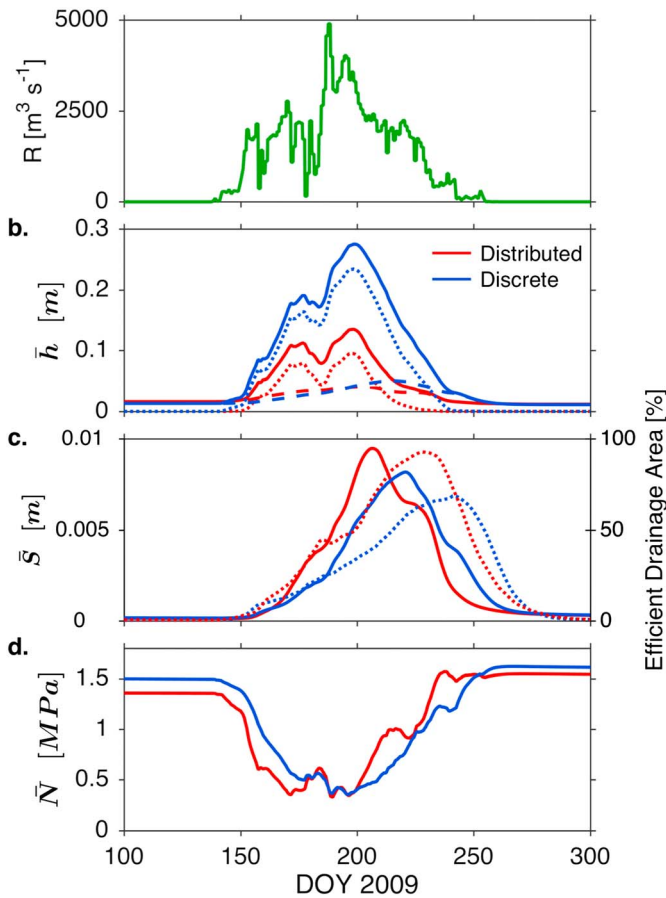
Figure 7. Differences in averaged model variables between the 2009 distributed (red) and discrete (blue) surface runoff input scenarios. (a) Surface runoff input integrated across the domain. (b) Average sheet height $\overline{h}$ across domain, with additional lines showing the contribution from the average cavity sheet height $\overline{h}_{cav}$ (dashed) and the average elastic sheet height $\overline{h}_{el}$ (dotted). (c) Average equivalent height of the channel layer $\overline{S}$ across the domain (solid lines) and the percentage of efficient drainage area of the TerraSAR-X region (dotted lines). Efficient drainage area is defined as the area within the TerraSAR-X region where effective pressure $N > 0$ MPa and total flux $q > 0.001$ m²/s. (d) Area-averaged effective pressures N across the domain. DOY = day of year.

efficient drainage increases (Figure 7c), effective pressures across the domain increase and eventually surpass their pre–melt season values (Figure 7d).

There are some important differences in the elastic sheet height, channel area, and discharge morphology between the distributed and discrete models with equivalent K_s, λ_c, and σ values. Over the melt season, the average height of the sheet layer h in the discrete model is roughly double that of the distributed model, with the majority of the height difference attributable to differences in elastic sheet height h_{el} (Figure 7b). The larger value of h_{el} in the discrete model is due to the focused, point source inputs of water, which result in local activation of the elastic sheet layer and more negative effective pressures at moulin sites in the early melt season (e.g., low N values at moulin locations on DOY 152 2009; Figure 5b). In contrast, the minimum effective pressures in the distributed model are less negative than the minimum effective pressures in the discrete model (Figure 5c), though negative effective pressures occur over a wider area in the distributed model (Figure 4c). Thus, while differences in surface runoff input between the two scenarios affect the distribution and magnitude of local effective pressures, these differences result in nearly equivalent minima in area-averaged effective pressures over the melt season (Figure 7d).

In the early melt season, *equivalent* channel height (i.e., the thickness of the channel layer if the channel volume was spread out over the entire grid cell) averaged across the domain increases faster in the distributed model compared to the discrete model (Figure 7c). For the same K_s, λ_c, and σ parameter values, the maximum total channel volume in the distributed input model precedes the discrete input model by 10–15 days (Figure 7c). Additionally, the maximum channel volume is larger in the distributed model (Figure 7c). These findings are consistent with the results of Banwell et al. (2016). In the distributed model, small channels can form at every node that is receiving surface melt, while channel formation in the discrete model is limited to nodes that are moulins or are down hydraulic potential from moulins. Thus, while the rate of total channel area growth is in part controlled by sheet layer permeability K_s and sheet layer width available for melting λ_c (equation (S8)), the rate of channel growth in the discrete input model is further limited by the larger horizontal distance between surface-to-bed meltwater pathways.

While locations of high subglacial discharge are similar between the two input scenarios by mid-melt season, routes of focused high discharge are more numerous in the discrete surface input model (Figures 4 and 5). For example, by DOY 218 2009, the discrete surface input model drainage system has ~10 routes to the margin with total fluxes $q > 0.1$ m²/s (Figure 5e), while the distributed surface input model drainage system has ~6 routes with total fluxes $q > 0.1$ m²/s (Figure 4e).

3.4. Relationship Between Surface Speeds and Driving Variables in 2009

To investigate the relationship between static variables (driving stress, bed elevation, surface slope, and ice sheet thickness) and evolving variables (surface runoff and effective pressure) and surface speeds in the region, we performed weighted linear regressions of the TerraSAR-X surface ice speeds against static and evolving variables (Figure 8). There is a significant positive relationship between surface speed and driving stress τ_d both in the winter and throughout the melt season (Figure 8). The remaining static variables exhibit varying relationships with surface speed over the melt season: bed elevation and surface slope show negative relationships with surface speeds in the mid-melt season but positive relationships for the remainder of the year (Figure S13); and ice thickness exhibits a slightly negative relationship with surface speed in the early melt season (Figure S13).
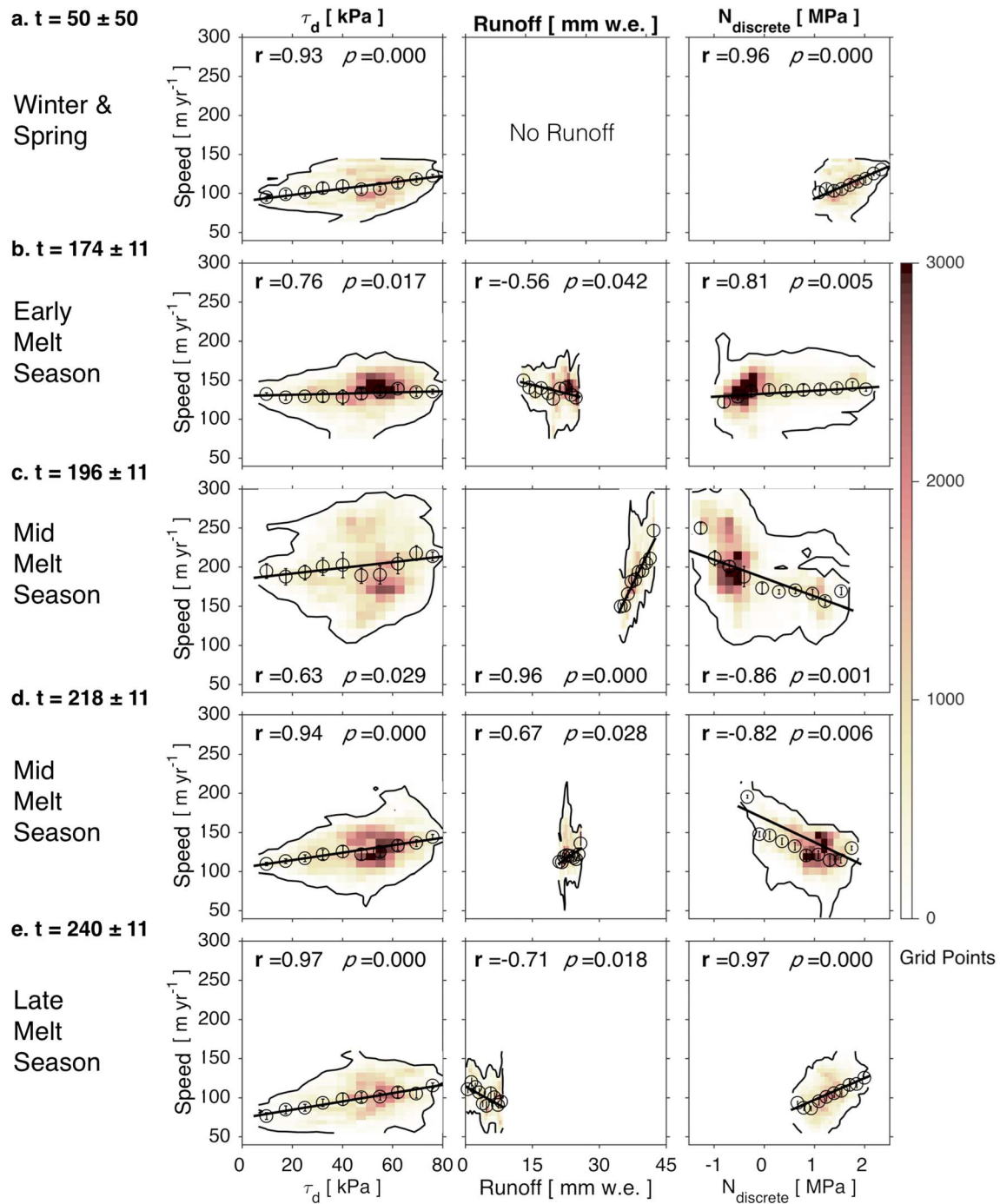
Figure 8. (a–e) Correlations with surface speeds evolve through the 2009 melt season. Runoff, driving stress τ_d, and model-derived 11-day averages of effective pressure N for a distributed and discrete input of surface forcing against the winter RADARSAT and melt season TerraSAR-X surface speed measurements. Data are linearly binned along the x and y axes, and the color of the bin represents the number of model grid points within that bin. Black contour surrounds data region with more than 10 model grid points. Surface speeds are averaged within each x axis bin (circles) and are fit with a weighted linear regression (black line), where the y value weights are two standard deviations (error bars). The weighted correlation coefficient **r** and the p value are derived from the weighted linear regression.

The sense of the relationships between surface speed and effective pressure and surface speed and runoff also varies over the melt season (Figure 8). Effective pressures and surface speed have a positive relationship in the winter, early, and late melt seasons but an inverse relationship in the mid-melt season (Figure 8). In
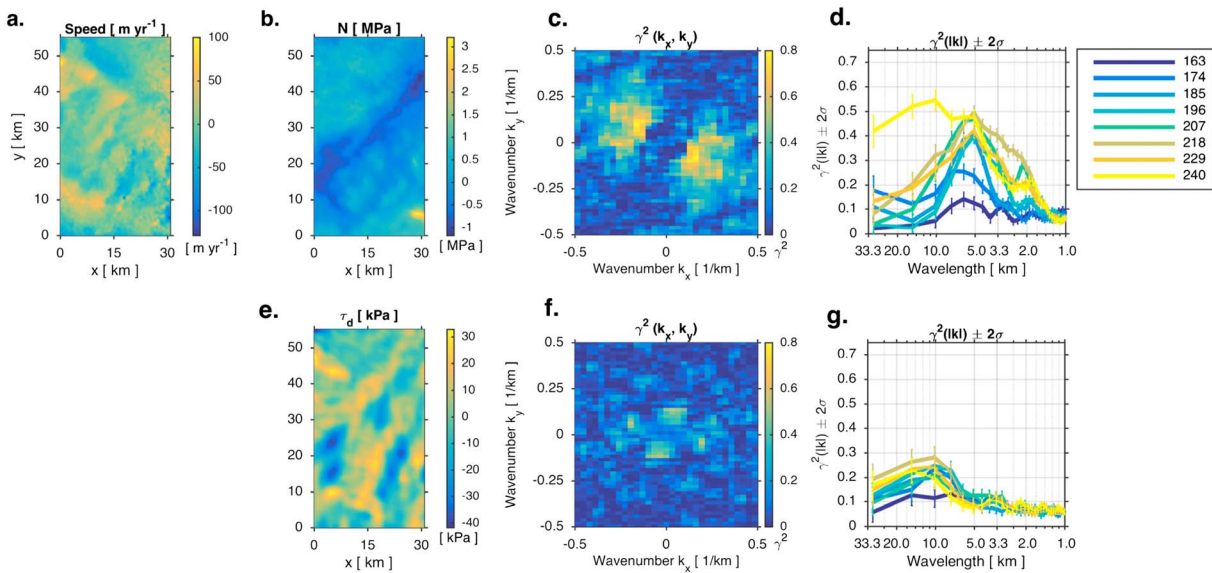
Figure 9. Coherence between speed and effective pressure and speed and driving stress on DOY 196 of 2009. Detrended and demeaned fields of 11-day averages centered on DOY 196 of 2009 of (a) surface ice speed and (b) modeled effective pressure N for a model with discrete surface runoff inputs. (c) The coherence-square estimates between fields (a) and (b) in wavenumber space, $\gamma^2(k_X, k_Y)$, where the smallest wavenumbers (largest, Rayleigh wavelengths) plot in the center of plot ($k_X = \lambda_R$, $k_Y = \lambda_R$), and the largest wavenumbers (smallest, Nyquist wavelengths) plot at the edges of the plot. The scale for the k_X and k_Y axes are linear in wavenumber. (d) The isotropically averaged coherence-square estimate, $\gamma^2(|k|) \pm 2\sigma$, between fields (a) and (b). The log x axis is equivalent to the axis in panel (c), but x axis tickmarks are now labeled in wavelength. (e–g) The equivalent coherence analysis as the first row of panels for (a) surface ice speed and (e) driving stress τ_d for the TerraSAR-X region. DOY = day of year.

contrast, runoff and surface speed have a positive relationship in the mid-melt season but an inverse relationship in the early and late melt seasons (Figure 8).

3.5. Relationship Between Surface Speeds and Driving Variables in 2010

Overall drainage system evolution and morphology are similar in 2010 as compared to 2009 between the respective distributed (Figure S10) and discrete (Figure S11) surface runoff models, with differences in channelization timing and extent driven by the longer duration melt season in 2010 (Figure S12a). A larger total runoff in 2010 results in greater sheet layer height h (Figure S12b) and lower area-averaged effective pressures compared to 2009 (Figure S12d). Area-averaged effective pressures are negative during the early and mid-melt seasons in the 2010 distributed model (Figure S12d) when runoff occurs across the entire model domain (Figure S10c–S10e).

Overall, the relationships observed in 2010 (Figure S14) are consistent with those seen in 2009, but with a few differences. In 2010, the slope of the relationships between surface speed and effective pressures again vary over the melt season (Figure S14). Effective pressure has a negative relationship with surface speed in the early and mid-melt seasons but a positive relationship in the late melt season and winter (Figure S14). The main difference between the two years is the lack of the positive relationship between effective pressure and speed in 2010 as was seen in the early melt season of 2009. Additionally, in 2010 runoff has a positive or insignificant relationship with surface speed in the early and mid-melt seasons (Figure S14), but a negative relationship at the end of the melt season (Figure 11c).

3.6. Coherence Estimates

We next examined the coherence between the static and evolving variables as described in section 2.3.3.. High coherence (>0.6) between speed and effective pressure in the northwest flowline direction (~270–315°) is observed on 2009 DOY 196 (Figure 9c), with a maximum in azimuthally averaged coherence at a wavelength of 5 km (Figure 9d). Similar maxima in azimuthally averaged coherence at a wavelength of 5 km between surface speed and effective pressures are found throughout the mid- and late-melt seasons in 2009 (Figure 9d). By contrast, surface speed shows lower coherence (~0.25) with driving stress throughout the 2009 melt season (Figure 9f) and at longer wavelengths (~10 km; Figure 9g). The stronger coherence
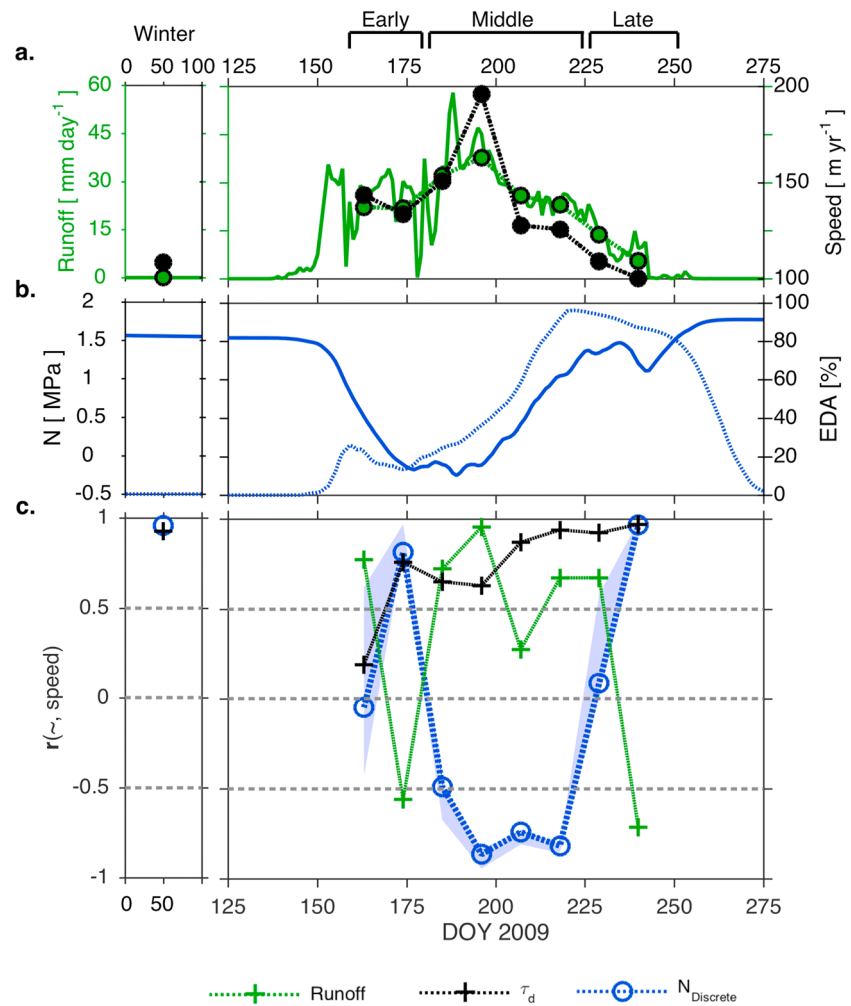
Figure 10. Linear and spectral relationships between runoff, driving stress τ_d, effective pressure, and surface speed evolve over the 2009 winter and melt season. (a) Daily (green line) and 11-day averages (green circle) of runoff over the TerraSAR-X region. Black circles are 11-day averages of TerraSAR-X surface speeds. (b) Daily effective pressure N and efficient drainage area over the TerraSAR-X region for models with discrete surface runoff input (blue). (c) Correlation coefficient, **r**, between TerraSAR-X speeds and effective pressure N for discrete (blue line) model run shown in Figure 5. Blue shading represents the maximum and minimum correlation coefficient across all models that meet the lake drainage criterion. Additional lines represent the correlation coefficient between TerraSAR-X speeds and runoff (green) and driving stress τ_d (black). EDA = efficient drainage area.

values between surface speed and effective pressures indicates that effective pressure driven by subglacial hydrology may more fully explain melt season speedup at shorter (~5 km) wavelengths, while driving stress may be more important for dictating broader scale ice flow at longer (≥10 km) wavelengths.

4. Discussion

4.1. Robust Subglacial Flow Pathways

Our simulations show similar overall drainage system morphology in 2009 and 2010 across both surface run-off input scenarios and much of the parameter space—with robust locations of high discharge forming in the same locations at the margin and under inland ice (Figures 4, 5, S10, and S11). In contrast to prior modeling studies suggesting that interior subglacial catchments switch ice margin outlet locations (Lindbäck et al., 2015; Chu et al., 2016), the positions of major drainage system pathways in our model remain stable throughout the melt season. This is likely because in our model channels grow inland from the ice sheet margin and channel growth affects the hydraulic potential field. Thus, once a channel is established, pressure lows
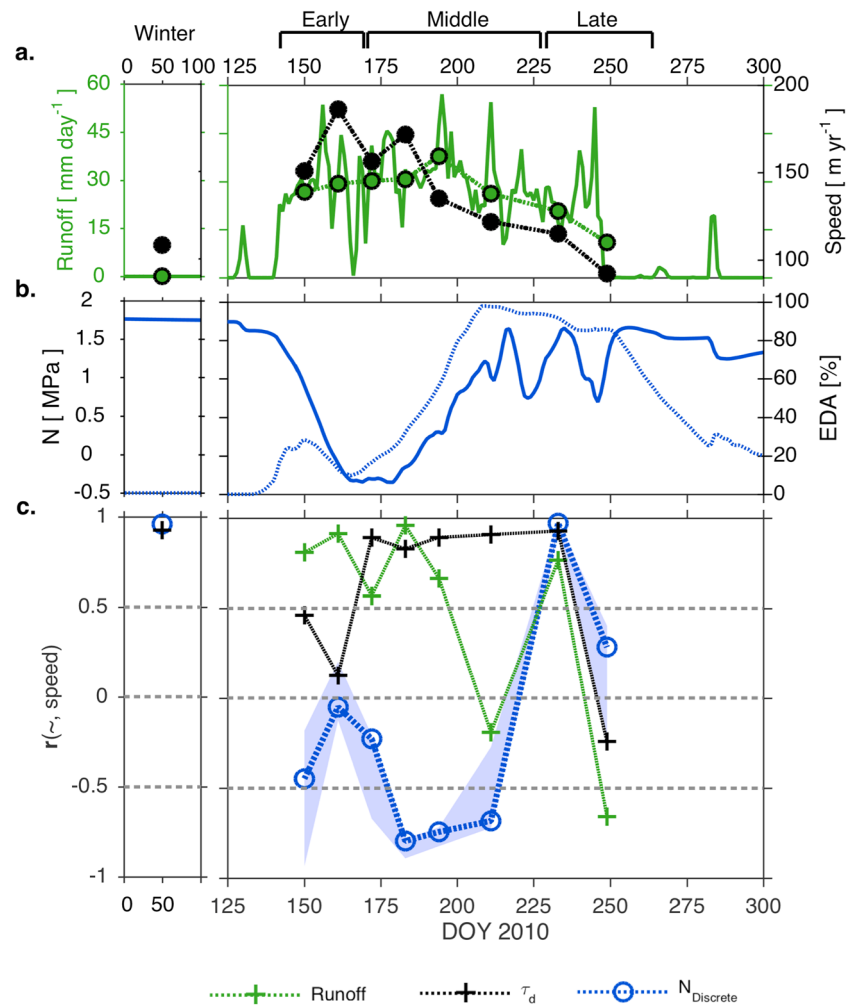
Figure 11. Linear and spectral relationships between runoff, driving stress τ_d, effective pressure, and surface speed evolve over the 2010 winter and melt season. The same as Figure 10 but for 2010. EDA = Efficient drainage area.

around the channel control the local hydraulic potential and steer water in the sheet layer toward the established channel (Hewitt, 2013; Werder et al., 2013).

Model output from both distributed and discrete input scenarios predicts subglacial channels grow across the major bedrock ridge in the model domain (Figure 1a), though the ridge does influence the orientation of channels on its southern margin (Figure 5d at $y = -20$ km in model space). Channel growth across this basal ridge is contradictory to static subglacial modeling of this area done by Stevens, Straneo, et al. (2016) and Chu et al. (2016), where subglacial drainage catchments were determined by steady state hydraulic potential fields. In those static models, catchments with outlets at the terminus of Sarqardleq or Alángordliup glaciers do not extend inland across the bedrock ridge except when water pressures are set above flotation across the entire region (Chu et al., 2016).

Channel growth across the bedrock ridge is also inconsistent with predictions of subglacial water pooling behind the bedrock ridge by Joughin et al. (2013). Based on observed summer velocities in 2009 and 2010, Joughin et al. (2013) suggested this ridge impedes basal water flow and leads to locally enhanced ice flow in the basal trough upstream of the bedrock ridge. Our modeling does predict that effective pressures are generally lower in the basal trough (Figure 9b); however, channels form across the bedrock ridge before the onset of locally enhanced ice flow in 2009 (Figures 4d and 5d) and shortly after the time of locally enhanced ice flow in 2010 (Figures S10d and S11d). Additionally, nearly all subglacial flow in the TerraSAR-X region is accommodated in the channel layer—as opposed to the sheet layer—by the late melt season.

Thus, while initial enhanced ice flow may be spatially concurrent with the lower effective pressures in the basal trough and spatiotemporally concurrent with supraglacial lake drainages, our results suggest that this water is evacuated from the basal trough within a matter of days or weeks.

The predicted drainage system morphology is unchanged with the inclusion of a pressure-dependent melting point for ice (Figure S16), which is neglected in the majority of our simulations. The pressure dependence of the melting point affects the evolution of subglacial channel size (equation (S7); Flowers, 2015) and can become important when water flowing up significant bed slopes freezes (Creyts & Clarke, 2010; Röthlisberger, 1972). In sensitivity tests, we found that although the rate of channelization for the distributed runoff input slows with the inclusion of the pressure dependence of the melting point, both the distributed and discrete models still grow channels with the same spatial patterns and across the major bedrock ridge separating the margin from the inland ice.

An important caveat to our results is the constant location of the imposed moulins in the discrete input scenario and the omission of supraglacial lake drainage events. Due to high moulin density at lower elevations, changing the number and/or location of moulins at low elevations is likely not so important for influencing low elevation channel locations. By contrast, adding new moulins above ~1,100 m above sea level where moulin density is much lower would likely influence channel development under inland ice. As moulins may persist for several years once formed (Catania et al., 2008), their advection away from their supraglacial water sources is another caveat to our results. Finally, the omission of supraglacial lake drainage events in the model may affect subglacial drainage efficiency and thus subglacial channel routing, as supraglacial lake drainage events have been shown to affect basal lubrication during and after drainage (Das et al., 2008; Hoffman et al., 2018).

4.2. Controls on Ice Sheet Margin Surface Speed Dynamics

The primary goal of this study is to investigate relationships between surface speed (as a proxy for basal sliding) and various parameters controlling ice dynamics (particularly effective pressure and driving stress). While measured surface speed reflects both basal sliding and internal deformation, borehole measurements suggest that basal sliding likely accounts for most of the surface motion during the summer (Ryser et al., 2014). We observe large changes in surface speed throughout the year that cannot be explained by variations in driving stress alone due to minor temporal changes in ice thickness or surface slope.

Based on the general form of most sliding models (Cuffey & Patterson, 2010; Fowler, 1987; Iken & Bindschadler, 1986; Schoof, 2010), we expect variations in effective pressure to be inversely related to changes in basal sliding speed at individual locations. Indeed, when keeping driving stress constant by selecting individual sites within the TerraSAR-X scenes, we lose the ability to look spatially but do find a negative relationship between model-derived effective pressures and TerraSAR-X speeds across the 2009 and 2010 melt season (Figure S17). Additionally, we expect variations in surface runoff to be positively related to surface speeds at the beginning of the melt season but then become negatively related to surface speeds by the end of the melt season as a channelized drainage network becomes established (Hoffman et al., 2011). The local driving stress also influences sliding speed and internal deformation, and we would expect a positive relationship between driving stress and surface speed across the study domain and at individual locations. However, the relationship between effective pressure and surface speeds over large areas may differ from the general form of sliding models due to spatial covariation between effective pressure, driving stress, and ice sheet bed conditions. By testing whether the inverse relationship between effective pressure and regional melt season surface speeds holds across a wide area, we can examine their spatial relationship between effective pressure and surface speed without the extra assumptions required when calculating surface speed from an ice flow model (e.g., Bougamont et al., 2014; de Fleurian et al., 2016; Hoffman & Price, 2014).

Throughout 2009 and 2010, a positive relationship between driving stress and surface speed is observed in both the winter and the melt season; an insignificant relationship between driving stress and surface speed is observed in the early and late 2010 melt seasons (Figure 11c). With the exception of a single inverse relationship between runoff and surface speed in the early melt season, a positive relationship is observed until the final TerraSAR-X scene on DOY 240 2009, which reverts to inverse relationship seen in the early melt season (Figure 11c). Further, our simulations predict an inverse relationship between effective pressure and surface

speed that is most akin to canonical models for basal sliding in the mid-melt season. In 2009, this inverse relationship (Figure 10c) occurs over consecutive TerraSAR-X 11-day intervals after surface speeds in the TerraSAR-X region have risen above ~150 m/year in the mid-melt season (Figure 10a). While the inverse relationship between surface speed and effective pressure could be interpreted to imply the nonlinear form expected for a sliding law relationship (Cuffey & Patterson, 2010; e.g., Figure 8c), we do not interpret the relationships beyond the significance and direction of a weighted linear fit because the magnitude of negative effective pressures calculated from the model partially depends on our choice of model parameters (equation (S5)). Outside the mid-melt season the relationship between effective pressure and speed is either positive (DOY 174 and 240) or insignificant (DOY 163 and 229; Figure 10c).

In 2010, the greatest surface speeds in the TerraSAR-X region occur in the early melt season (Figure 11a), and an inverse relationship between effective pressure and speed occurs in both the early and mid-melt seasons (Figure 11c). These varying relationships between surface speed and effective pressure over the melt season are found across a wide range of parameters (shading in Figures 10c and 11c).

There are a number of reasons that we may see different relationships between effective pressure and surface speed in the early and late melt seasons as compared to the mid-melt season. First, our hydrologic model may be missing some aspect of the physics that dictates effective pressure, resulting in a poor depiction of the subglacial system in the early and late melt seasons. For example, we have not included a surface storage term for runoff. Storage of meltwater in the snowpack and/or supraglacial lakes would result in a lag in the timing of runoff access to the bed (de Fleurian et al., 2016; Joughin et al., 2013). As runoff in our model is prescribed to immediately transit to the basal environment, we may observe a positive relationship between effective pressure and surface speed in the early melt season due to runoff accessing the bed too quickly in our model. In the late melt season, the positive relationship between effective pressure and surface speed may result from lack of a disconnected or weakly connected component of the subglacial drainage system in the model (Andrews et al., 2014; Hoffman et al., 2016). By not resolving these isolated components of the bed, we are effectively modeling the effective pressure only in the connected system. Thus, our modeled effective pressures for the connected drainage system may not be the relevant effective pressures for comparing against ice speeds in the late melt season if the weakly connected component of the subglacial drainage system controls ice speeds during this time as proposed by Andrews et al. (2014) and Hoffman et al. (2016). In these scenarios, the observed positive relationship would be an artifact of our model assumptions and limitations rather than a true reflection of the behavior of the system.

Second, the positive relationship between effective pressure and surface speed at the start and end of the melt season may suggest that the influence of effective pressure on surface speed is masked by the influence of spatially variable driving stress and bed roughness outside of the mid-melt season. We find that effective pressure and driving stress are positively correlated outside of the mid-melt season, likely due to the influence of ice sheet thickness on both the driving stress and ice overburden pressure. As noted above, when holding driving stress constant, we do see an inverse relationship between modeled effective pressure and speed for individual locations within the TerraSAR-X scenes (Figure S17). Thus, the positive spatial relationship between effective pressure and surface speed during the start and end of the melt season may be primarily related to covariance with the driving stress rather than effective pressure alone.

4.3. Coherence Estimates

Two-dimensional coherence estimates proved a useful tool to compare variability across wavelengths between surface speeds, static variables, and modeled effective pressures. These coherence estimates suggest that both long- (>10 km) and short-wavelength (<3 km) variability in effective pressure variability are not reflected in surface speed; however, high coherence between effective pressure and surface speed is observed at intermediate wavelengths (3–10 km), peaking at a wavelength of ~5 km. Additionally, we find that the directionality of the coherence between surface speed and effective pressure is maximized in the flowline direction. Thus, there appears to be both a wavelength and azimuthal dependence in the ability of effective pressure to control surface speed.

With the rapid increase in high temporal and spatial resolution surface speed measurements (Fahnestock et al., 2015; Mouginot et al., 2017), future studies can extend two-dimensional coherence estimation to larger regions of the ice sheet and may also prove useful for planning instrument arrays in the field. For example,

coherence estimates of wavelength dependence for driving stress, bed topography, and effective pressure could identify the ideal spacing for surface measurements of ice flow and/or bed measurements of subglacial systems. Additionally, wavelength and azimuthal dependence of coherence estimates between ice sheet flow and bed topography may be useful for constraining over what scales and directions bed topography dictates ice flow.

4.4. Model Limitations

The hydrology model used here has limitations that affect the magnitude of effective pressure. At present, the model handles large injections of meltwater poorly, resulting in unrealistically low effective pressures. Proper handling of flexural bending stresses in the elastic sheet layer h_{el} must be added to the model to prevent unrealistically high water pressures at moulin nodes where discrete meltwater inputs occur. As such, an important caveat in the interpretation of our model results is that although the transition from positive to negative effective pressures is a robust prediction of the model, the magnitude of effective pressure is sensitive to the uplift compliance (C_{el}) and regularizing pressure (N_0) assumed in the model (equation (S5)). Thus, the absolute values of effective pressure should be interpreted with caution, but differences in these values between model runs that employ the same values for C_{el} and N_0 are likely significant.

The model could be further improved by adding a disconnected or weakly connected component of the drainage system to better represent regions of the bed that become isolated from the larger drainage system over the melt season but remain important for ice flow (Andrews et al., 2014; Hoffman et al., 2016). The addition of a disconnected component of the drainage system may also better reproduce high winter basal water pressures often observed in boreholes (Andrews et al., 2014; Flowers, 2015; Hoffman et al., 2016; Wright et al., 2016).

Finally, the model forcing could be improved by making the timing and rate of surface runoff inputs to the bed increasingly more realistic. We could employ a storage of meltwater in the snowpack to lag the timing of runoff to the bed at the start of the season (de Fleurian et al., 2016), and/or we could specify different mechanisms and rates at which supraglacial water travels to the bed (Banwell et al., 2013, 2016; Hoffman et al., 2018; Koziol et al., 2017). Whether these improvements to the hydrology model would result in more realistic timing of the switch to negative effective pressures in the early melt season will be the focus of future studies.

4.5. Future Directions

While many improvements to the model can still be made (section 4.1), efforts to validate coupled subglacial hydrology and ice flow models with new observations are critical for advancing our understanding of these systems (Flowers, 2015). Ice sheet surface speed measurements at increasingly high temporal and spatial resolutions are now available with the launch of the Sentinel-1 and Landsat-8 satellites (Fahnestock et al., 2015; Mouginot et al., 2017). With large coverage in both space and time, these measurements will enable improved testing of the dependence of subglacial hydrology on the sliding law. Finally, although our estimates of effective pressure are only model predictions, our simulations suggest that some aspects of melt season surface speeds are consistent with the inclusion of an effective pressure term in the sliding law. As it is not currently feasible to measure basal water pressures at the temporal and spatial scales necessary to force a regional ice sheet model, future studies must continue to use hydrology models to estimate effective pressure in order for pressure-dependent sliding laws to be implemented in ice sheet models.

5. Conclusions

Using a numerical model of subglacial hydrology, we investigate how model-derived effective pressures relate to the complex spatiotemporal pattern of surface speed observed over the 2009 and 2010 melt seasons. We find similar relationships between effective pressure and surface speed for both distributed and discrete surface runoff input across a wide range of model parameters. Overall drainage system morphology is similar in both years, with robust subglacial pathways forming over bedrock ridges and not being confined to bedrock lows, in contrast to prior model predictions in this region. Consistently across 2009 and 2010, our results show an inverse relationship between effective pressure and speed when surface speeds are high in the mid-melt season. By contrast, in the early and late melt seasons, effective pressure and speed have a positive relationship. During these periods of slower ice motion, driving stress and spatially variable bed

roughness may influence sliding speed more than effective pressure. Future work should continue to compare models of subglacial water drainage with local and regional surface speed, and also with actual observations of effective pressure. These investigations will help identify further model advances necessary for improving our ability to predict dynamic ice changes.

References

Andrews, L. C., Catania, G. A., Hoffman, M. J., Gulley, J. D., Lüthi, M. P., Ryser, C., et al. (2014). Direct observations of evolving subglacial drainage beneath the Greenland Ice Sheet. *Nature*, *514*(7520), 80–83. https://doi.org/10.1038/nature13796

Bamber, J. L., Griggs, J. A., Hurkmans, R. T. W. L., Dowdeswell, J. A., Gogineni, S. P., Howat, I., et al. (2013). A new bed elevation dataset for Greenland. *The Cryosphere*, *7*, 499–510. https://doi.org/10.5194/tc-7-499-2013

Banwell, A., Hewitt, I., Willis, I., & Arnold, N. (2016). Moulin density controls drainage development beneath the Greenland ice sheet. *Journal of Geophysical Research: Earth Surface*, *121*, 2248–2269. https://doi.org/10.1002/2015JF003801

Banwell, A. F., Willis, I., & Arnold, N. (2013). Modeling subglacial water routing at Paakitsoq, W Greenland. *Journal of Geophysical Research: Earth Surface*, *118*, 1282–1295. https://doi.org/10.1002/jgrf.20093

Bartholomaus, T. C., Anderson, R. S., & Anderson, S. P. (2011). Growth and collapse of the distributed subglacial hydrologic system of Kennicott Glacier, Alaska, USA, and its effects on basal motion. *Journal of Glaciology*, *57*(206), 985–1002. https://doi.org/10.3189/002214311798843269

Bendat, J. S., & Piersol, A. G. (1993). *Engineering applications of correlation and spectral analysis* (2nd ed.). New York: John Wiley.

Bougamont, M., Christoffersen, P., Hubbard, A. L., Fitzpatrick, A. A., Doyle, S. H., & Carter, S. P. (2014). Sensitive response of the Greenland ice sheet to surface melt drainage over a soft bed. *Nature Communications*, *5*(1), 5052. https://doi.org/10.1038/ncomms6052

Catania, G. A., Neumann, T. A., & Price, S. F. (2008). Characterizing englacial drainage in the ablation zone of the Greenland ice sheet. *Journal of Glaciology*, *54*(187), 567–578. https://doi.org/10.3189/002214308786570854

Chu, V. W. (2013). Greenland ice sheet hydrology: A review. *Progress in Physical Geography*, *1*, 1–36. https://doi.org/10.1177/0309133313507075

Chu, W., Creyts, T. T., & Bell, R. E. (2016). Rerouting of subglacial water flow between neighboring glaciers in West Greenland. *Journal of Geophysical Research: Earth Surface*, *121*, 1–14. https://doi.org/10.1002/2015JF003705

Creyts, T. T., & Clarke, G. K. C. (2010). Hydraulics of subglacial supercooling: Theory and simulations for clear water flows. *Journal of Geophysical Research*, *115*, F03021. https://doi.org/10.1029/2009JF001417

Creyts, T. T., & Schoof, C. G. (2009). Drainage through subglacial water sheets. *Journal of Geophysical Research*, *114*, F04008. https://doi.org/10.1029/2008JF001215

Cuffey, K. M., & Patterson, W. S. B. (2010). *The physics of glaciers* (4th ed.). Burlington, MA: Elsevier.

Das, S. B., Joughin, I., Behn, M. D., Howat, I. M., King, M. A., Lizarralde, D., & Bhatia, M. P. (2008). Fracture propagation to the base of the Greenland ice sheet during supraglacial lake drainage. *Science*, *320*(5877), 778–781. https://doi.org/10.1126/science.1153360

de Fleurian, B., Morlighem, M., Seroussi, H., Rignot, E., van den Broeke, M. R., Kuipers Munneke, P., et al. (2016). A modeling study of the effect of runoff variability on the effective pressure beneath Russell Glacier, West Greenland. *Journal of Geophysical Research: Earth Surface*, *121*, 1834–1848. https://doi.org/10.1002/2016JF003842

Fahnestock, M., Scambos, T., Moon, T., Gardner, A., Haran, T., & Klinger, M. (2015). Rapid large-area mapping of ice flow using Landsat 8. *Remote Sensing of Environment*, *185*(2016), 84–94. https://doi.org/10.1016/j.rse.2015.11.023

Flowers, G. E. (2015). Modelling water flow under glaciers and ice sheets. *Proceeding of the Royal Society A Mathematical, Physical and Engineering Sciences*, *471*, 1–41.

Forsyth, D. W. (1985). Subsurface loading and estimates of the flexural rigidity of continental lithosphere. *Journal of Geophysical Research*, *90*(B14), 12,623–12,632. https://doi.org/10.1029/JB090iB14p12623

Fowler, A. C. (1987). Sliding with cavity formation. *Journal of Glaciology*, *33*(115), 255–267. https://doi.org/10.1017/S0022143000008820

Harper, J. T., Bradford, J. H., Humphrey, N. F., & Meierbachtol, T. W. (2010). Vertical extension of the subglacial drainage system into basal crevasses. *Nature*, *467*(7315), 579–582. https://doi.org/10.1038/nature09398

Hewitt, I. J. (2013). Seasonal changes in ice sheet motion due to melt water lubrication. *Earth and Planetary Science Letters*, *371*, 16–25. https://doi.org/10.1016/j.epsl.2013.04.022

Hewitt, I. J., Schoof, C., & Werder, M. A. (2012). Flotation and free surface flow in a model for subglacial drainage. Part 2. Channel flow. *Journal of Fluid Mechanics*, *702*, 157–187. https://doi.org/10.1017/jfm.2012.166

Hoffman, M., & Price, S. (2014). Feedbacks between coupled subglacial hydrology and glacier dynamics. *Journal of Geophysical Research: Earth Surface*, *119*, 414–436. https://doi.org/10.1002/2013JF002943

Hoffman, M. J., Andrews, L. C., Price, S. A., Catania, G. A., Neumann, T. A., Luethi, M. P., et al. (2016). Greenland subglacial drainage evolution regulated by weakly-connected regions of the bed. *Nature Communications*, *7*, 13,903. https://doi.org/10.1038/ncomms13903

Hoffman, M. J., Catania, G. A., Neumann, T. A., Andrews, L. C., & Rumrill, J. A. (2011). Links between acceleration, melting, and supraglacial lake drainage of the western Greenland ice sheet. *Journal of Geophysical Research*, *116*, F04035. https://doi.org/10.1029/2010JF001934

Hoffman, M. J., Perego, M., Andrews, L. C., Catania, G., Price, S. F., Lüthi, M. P., et al. (2018). Widespread moulin formation during supraglacial lake drainages in Greenland. *Geophysical Research Letters*, *45*, 778–788. https://doi.org/10.1002/2017GL075659

Howat, I. M., Negrete, A., & Smith, B. E. (2014). The Greenland Ice Mapping Project (GIMP) land classification and surface elevation data sets. *The Cryosphere*, *8*(4), 1509–1518. https://doi.org/10.5194/tc-8-1509-2014

Iken, A., & Bindschadler, R. A. (1986). Combined measurements of subglacial water pressure and surface velocity of Findelengletscher, Switzerland: Conclusions about drainage system and sliding mechanism. *Journal of Glaciology*, *32*(110), 101–119. https://doi.org/10.1017/S0022143000006936

Joughin, I., Das, S. B., Flowers, G. E., Behn, M. D., Alley, R. B., King, M. A., et al. (2013). Influence of ice-sheet geometry and supraglacial lakes on seasonal ice-flow variability. *The Cryosphere*, *7*(4), 1185–1192. https://doi.org/10.5194/tc-7-1185-2013

Joughin, I., Das, S. B., King, M. A., Smith, B. E., Howat, I. M., & Moon, T. (2008). Seasonal speedup along the western flank of the Greenland ice sheet. *Science*, *320*(5877), 781–783. https://doi.org/10.1126/science.1153288

Joughin, I., Smith, B., & Howat, I. (2017). A complete map of Greenland ice velocity derived from satellite data collected over 20 years, *Journal of Glaciology*. 1–11. https://doi.org/10.1017/jog.2017.73

Joughin, I., Smith, B., Howat, I., & Scambos, T. (2016). MEaSUREs Multi-year Greenland Ice Sheet Velocity Mosaic, Version 1. Boulder, CO. NASA National Snow and Ice Data Center Distributed Active Archive Center. https://doi.org/https://doi.org/10.5067/QUA5Q9SVMSJG

Joughin, I., Smith, B. E., Howat, I. M., Scambos, T., & Moon, T. (2010). Greenland flow variability from ice-sheet-wide velocity mapping. *Journal of Glaciology*, *56*(197), 415–430. https://doi.org/10.3189/002214310792447734

Kirby, J. F. (2014). Estimation of the effective elastic thickness of the lithosphere using inverse spectral methods: The state of the art. *Tectonophysics*, *631*(C), 87–116. https://doi.org/10.1016/j.tecto.2014.04.021

Koziol, C., Arnold, N. S., Pope, A., & Colgan, W. (2017). Quantifying supraglacial meltwater pathways in the Paakitsoq Region, West Greenland. *Journal of Glaciology*, *63*(239), 464–476. https://doi.org/10.1017/jog.2017.5

Lindbäck, K., Pettersson, R., Hubbard, A. L., Doyle, S. H., As, D., Mikkelsen, A. B., & Fitzpatrick, A. A. (2015). Subglacial water drainage, storage, and piracy beneath the Greenland ice sheet. *Geophysical Research Letters*, *42*, 7606–7614. https://doi.org/10.1002/2015GL065393

Morlighem, M., Rignot, E., Mouginot, J., Seroussi, H., & Larour, E. (2014). Deeply incised submarine glacial valleys beneath the Greenland ice sheet. *Nature Geoscience*, *7*(6), 418–422. https://doi.org/10.1038/ngeo2167

Mouginot, J., Rignot, E., Scheuchl, B., & Millan, R. (2017). Comprehensive annual ice sheet velocity mapping using Landsat-8, Sentinel-1, and RADARSAT-2 data. *Remote Sensing*, *9*(4), 1–20. https://doi.org/10.3390/rs9040364

Noël, B., van de Berg, W. J., Machguth, H., Lhermitte, S., Howat, I., Fettweis, X., & van den Broeke, M. R. (2016). A daily, 1 km resolution data set of downscaled Greenland ice sheet surface mass balance (1958–2015). *The Cryosphere*, *10*(5), 2361–2377. https://doi.org/10.5194/tc-10-2361-2016

Noël, B., van de Berg, W. J., van Meijgaard, E., Kuipers Munneke, P., van de Wal, R. S. W., & van den Broeke, M. R. (2015). Evaluation of the updated regional climate model RACMO2.3: Summer snowfall impact on the Greenland Ice Sheet. *The Cryosphere*, *9*(5), 1831–1844. https://doi.org/10.5194/tc-9-1831-2015

Palmer, S., Shepherd, A., Nienow, P., & Joughin, I. (2011). Seasonal speedup of the Greenland ice sheet linked to routing of surface water. *Earth and Planetary Science Letters*, *302*(3–4), 423–428. https://doi.org/10.1016/j.epsl.2010.12.037

Pimentel, S., & Flowers, G. E. (2010). A numerical study of hydrologically driven glacier dynamics and subglacial flooding. *Proceeding of the Royal Society A Mathematical, Physical and Engineering Sciences*, *467*(2126), 537–558. https://doi.org/10.1098/rspa.2010.0211

Poinar, K., Joughin, I., Lenaerts, J. T. M., & van den Broeke, M. R. (2016). Englacial latent-heat transfer has limited influence on seaward ice flux in western Greenland. *Journal of Glaciology*, *63*(237), 1–16. https://doi.org/10.1017/jog.2016.103

Pritchard, H. D., Arthern, R. J., Vaughan, D. G., & Edwards, L. A. (2009). Extensive dynamic thinning on the margins of the Greenland and Antarctic ice sheets. *Nature*, *461*(7266), 971–975. https://doi.org/10.1038/nature08471

Rogozhina, I., Hagedoorn, J. M., Martinec, Z., Fleming, K., Soucek, O., Greve, R., & Thomas, M. (2012). Effects of uncertainties in the geothermal heat flux distribution on the Greenland ice sheet: An assessment of existing heat flow models. *Journal of Geophysical Research*, *117*, F02025. https://doi.org/10.1029/2011JF002098

Röthlisberger, H. (1972). Water pressure in intra- and subglacial channels. *Journal of Glaciology*, *11*(62), 177–203. https://doi.org/10.1017/S0022143000022188

Ryser, C., Lüthi, M. P., Andrews, L. C., Hoffman, M. J., Catania, G. A., Hawley, R. L., et al. (2014). Sustained high basal motion of the Greenland ice sheet revealed by borehole deformation. *Journal of Glaciology*, *60*(222), 647–660. https://doi.org/10.3189/2014JoG13J196

Schoof, C. (2010). Ice-sheet acceleration driven by melt supply variability. *Nature*, *468*(7325), 803–806. https://doi.org/10.1038/nature09618

Schoof, C., Hewitt, I. J., & Werder, M. A. (2012). Flotation and free surface flow in a model for subglacial drainage. Part 1. Distributed drainage. *Journal of Fluid Mechanics*, *702*, 126–156. https://doi.org/10.1017/jfm.2012.165

Seymour, M. S., & Cumming, I. G. (1994). Maximum likelihood estimation for SAR interferometry. *Proceedings of the International Geoscience and Remote Sensing Symposia*, *4*, 2272–2275.

Shepherd, A., Hubbard, A., Nienow, P., King, M., Mcmillan, M., & Joughin, I. (2009). Greenland ice sheet motion coupled with daily melting in late summer. *Geophysical Research Letters*, *36*, L01501. https://doi.org/10.1029/2008GL035758

Simons, F. J., van der Hilst, R. D., & Zuber, M. T. (2003). Spatiospectral localization of isostatic coherence anisotropy in Australia and its relation to seismic anisotropy: Implications for lithospheric deformation. *Journal of Geophysical Research*, *108*(B5), 2250. https://doi.org/10.1029/2001JB000704

Simons, J., Zuber, M. T., & Korenaga, J. (2000). Isostatic response of the Australian lithosphere: Estimation of effective elastic thickness and anisotropy using multitaper spectral analysis. *Journal of Geophysical Research*, *105*(B8), 19,163–19,184. https://doi.org/10.1029/2000JB900157

Slepian, D. (1978). Prolate spheroidal wave functions, Fourier analysis, and uncertainty. V—The discrete case. *Bell Labs Technical Journal*, *57*(5), 1371–1430. https://doi.org/10.1002/j.1538-7305.1978.tb02104.x

Smith, L. C., Chu, V. W., Yang, K., Gleason, C. J., Pitcher, L. H., Rennermalm, A. K., et al. (2015). Efficient meltwater drainage through supraglacial streams and rivers on the southwest Greenland ice sheet. *Proceedings of the National Academy of Sciences*, *112*(4), 1001–1006. https://doi.org/10.1073/pnas.1413024112

Sole, A., Nienow, P., Bartholomew, I., Mair, D., Cowton, T., Tedstone, A., & King, M. A. (2013). Winter motion mediates dynamic response of the Greenland Ice Sheet to warmer summers. *Geophysical Research Letters*, *40*, 3940–3944. https://doi.org/10.1002/grl.50764

Stevens, L. A., Behn, M. D., Das, S. B., Joughin, I., Noël, B. P. Y., van den Broeke, M. R., & Herring, T. (2016). Greenland Ice Sheet flow response to runoff variability. *Geophysical Research Letters*, *43*, 11,295–11,303. https://doi.org/10.1002/2016GL070414

Stevens, L. A., Behn, M. D., McGuire, J. J., Das, S. B., Joughin, I., Herring, T., et al. (2015). Greenland supraglacial lake drainages triggered by hydrologically induced basal slip. *Nature*, *522*(7554), 73–76. https://doi.org/10.1038/nature14480

Stevens, L. A., Straneo, F., Das, S. B., Plueddemann, A. J., & Kukulya, A. L. (2016). Linking glacially modified waters to catchment-scale subglacial discharge using autonomous underwater vehicle observations. *The Cryosphere*, *10*(1), 417–432. https://doi.org/10.5194/tc-10-417-2016

Tedstone, A. J., Nienow, P. W., Gourmelen, N., Dehecq, A., Goldberg, D., & Hanna, E. (2015). Decadal slowdown of a land-terminating sector of the Greenland Ice Sheet despite warming. *Nature*, *526*(7575), 692–695. https://doi.org/10.1038/nature15722

Thomson, D. J. (1982). Spectrum estimation and harmonic analysis. *Proceeding IEEE*, *70*, 1055–1096.

van de Wal, R. S. W., Boot, W., van den Broeke, M. R., Smeets, C. J. P. P., Reijmer, C. H., Donker, J. J. A., & Oerlemans, J. (2008). Large and rapid melt-induced velocity changes in the ablation zone of the Greenland Ice Sheet. *Science*, *321*(5885), 111–113. https://doi.org/10.1126/science.1158540

van de Wal, R. S. W., Smeets, C. J. P. P., Boot, W., Stoffelen, M., van Kampen, R., Doyle, S., et al. (2015). Self-regulation of ice flow varies across the ablation area in south-west Greenland. *The Cryosphere*, *9*, 603–611. https://doi.org/10.5194/tc-9-603-2015

Vaughan, D. G., Comiso, J. C., Allison, I., Carrasco, J., Kaser, G., Kwok, R., et al. (2013). Observations: Cryosphere. Climate change 2013: The physical science basis. In *Contribution of Working Group I to the Fifth Assessment Report of the Intergovernmental Panel on Climate Change* (pp. 317–382). Cambridge, UK. https://doi.org/10.1017/CBO9781107415324.012

Werder, M. A., Hewitt, I. J., Schoof, C. G., & Flowers, G. E. (2013). Modeling channelized and distributed subglacial drainage in two dimensions. *Journal of Geophysical Research: Earth Surface*, *118*, 2140–2158. https://doi.org/10.1002/jgrf.20146

Wright, P. J., Harper, J. T., Humphrey, N. F., & Meierbachtol, T. W. (2016). Measured basal water pressure variability of the western Greenland Ice Sheet: Implications for hydraulic potential. *Journal of Geophysical Research: Earth Surface*, *121*, 1–14. https://doi.org/10.1002/2016JF003819

Yang, K., Smith, L. C., Chu, V. W., Gleason, C. J., & Li, M. (2015). A caution on the use of surface digital elevation models to simulate supraglacial hydrology of the Greenland ice sheet. *IEEE Journal of Selected Topics in Applied Earth Observations and Remote Sensing*, *8*(11), 5212–5224. https://doi.org/10.1109/JSTARS.2015.2483483

Zwally, H. J., Abdalati, W., Herring, T., Larson, K., Saba, J., & Steffen, K. (2002). Surface melt-induced acceleration of Greenland ice-sheet flow. *Science*, *297*(5579), 218–222. https://doi.org/10.1126/science.1072708